



Title	High-n ballooning instabilities in toroidally rotating tokamaks
Author(s)	Furukawa, M.; Nakamura, Yuji; Hamaguchi, S. et al.
Citation	Physics of Plasmas. 2001, 8(11), p. 4889-4897
Version Type	VoR
URL	<a href="https://hdl.handle.net/11094/78491">https://hdl.handle.net/11094/78491</a>
rights	This article may be downloaded for personal use only. Any other use requires prior permission of the author and AIP Publishing. This article appeared in Physics of Plasmas 8, 4889 (2001) and may be found at <a href="https://doi.org/10.1063/1.1410382">https://doi.org/10.1063/1.1410382</a> .
Note	

*The University of Osaka Institutional Knowledge Archive : OUKA*

<https://ir.library.osaka-u.ac.jp/>

The University of Osaka

# High- $n$ ballooning instabilities in toroidally rotating tokamaks

Cite as: Physics of Plasmas **8**, 4889 (2001); <https://doi.org/10.1063/1.1410382>

Submitted: 07 May 2001 . Accepted: 21 August 2001 . Published Online: 19 October 2001

M. Furukawa, Yuji Nakamura, S. Hamaguchi, and M. Wakatani



View Online



Export Citation

## ARTICLES YOU MAY BE INTERESTED IN

[Magnetohydrodynamic stability of tokamak edge plasmas](#)

Physics of Plasmas **5**, 2687 (1998); <https://doi.org/10.1063/1.872956>

[Ballooning mode spectrum in general toroidal systems](#)

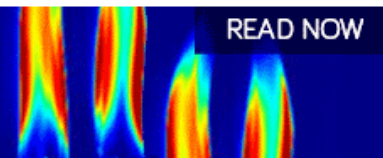
The Physics of Fluids **26**, 3038 (1983); <https://doi.org/10.1063/1.864028>

[Magnetic reconnection via current sheets](#)

The Physics of Fluids **29**, 1520 (1986); <https://doi.org/10.1063/1.865670>

AIP Advances  
Fluids and Plasmas Collection

READ NOW



# High- $n$ ballooning instabilities in toroidally rotating tokamaks

M. Furukawa,<sup>a)</sup> Yuji Nakamura, S. Hamaguchi, and M. Wakatani  
*Graduate School of Energy Science, Kyoto University, Gokasho, Uji 611-0011, Japan*

(Received 7 May 2001; accepted 21 August 2001)

High- $n$  ballooning instabilities are studied with an initial-value code for toroidally rotating tokamaks, where  $n$  is a toroidal mode number. The effects of toroidal rotation are classified into two parts: (i) increase of effective pressure gradient due to the centrifugal force of the toroidal flow, and (ii) averaging of local magnetic equilibrium configuration over a period of poloidal angle in the case of finite flow-velocity shear. With the increase of effective pressure gradient in the rigid-rotation case, the growth rate of ballooning mode increases in the low-pressure regime as the toroidal flow velocity is increased, whereas it decreases in the high-pressure regime. The flow-velocity shear generally reduces the growth rate of the high- $n$  ballooning mode by the averaging of the local equilibrium magnetic configuration. However, it is found that the ballooning mode becomes unstable by increasing the flow-velocity shear in a low-aspect-ratio tokamak. This is understood by the change of the local magnetic configuration, and by the changes of both the mode structure and the potential function in the ballooning space. © 2001 American Institute of Physics. [DOI: 10.1063/1.1410382]

## I. INTRODUCTION

In recent tokamak experiments, substantial plasma flows have been observed,<sup>1–3</sup> particularly when the confinement improvement has been realized in the H(high)-mode plasmas or in negative shear configurations with the internal transport barrier. The flows have both toroidal and poloidal components in general, although toroidal flows seem to be dominant in the core region of the plasmas. In order to realize an advanced tokamak, high bootstrap current is required in a negative shear configuration. For increasing the bootstrap current, a high-beta-poloidal plasma is essential. Therefore, effects of toroidal flows on high- $n$  ballooning instabilities are studied here, where  $n$  is a toroidal mode number.

The theory on high- $n$  ballooning modes without plasma flows is well established.<sup>4–6</sup> An eikonal representation or ballooning representation is introduced for ballooning perturbations in these papers. For tokamak plasmas including toroidal flows, Cooper has used a time-dependent eikonal to represent the ballooning perturbation, and has solved the incompressible high- $n$  ballooning equations as an initial-value problem.<sup>7</sup> The obtained solution exhibits a periodically modulated exponential growth of perturbed energy, which has been explained by Hameiri and Chun as a consequence of the periodicity of the coefficients of the ballooning equations in the coordinates drifting along the magnetic field line.<sup>8</sup> Compressible high- $n$  ballooning equations were derived by Waelbroeck and Chen,<sup>9</sup> and by Grassie and Krech.<sup>10</sup> In Ref. 9, they have shown the transformation formula between the eikonal solution and the eigenmode solution. Furthermore, Miller *et al.*<sup>11</sup> and Grassie and Krech<sup>12</sup> have simplified the compressible high- $n$  ballooning equations with the toroidal flow for shifted-circle equilibria given by

Shafranov,<sup>13</sup> and have solved them numerically. In Ref. 11, they have shown a generalized  $s$ - $\alpha$  diagram, and found that the unstable region may be reduced significantly by the flow-velocity shear.

In the present article, the compressible high- $n$  ballooning equations including the toroidal flow are solved numerically as an initial-value problem, and obtained results are shown. The magnetohydrodynamic (MHD) equilibria with toroidal flows are given numerically,<sup>14</sup> therefore consistency between the equilibrium and the stability of ballooning mode is kept. In Sec. II, a MHD equilibrium equation for tokamaks including toroidal flows is introduced.<sup>15</sup> The compressible high- $n$  ballooning equations including toroidal flows are also introduced in Sec. II. Brief derivation of the ballooning equations is given in the Appendix. The effects of toroidal flows are classified into two parts: (i) the effective pressure gradient due to the centrifugal force of the toroidal flow, and (ii) the averaging of the local equilibrium magnetic configuration due to the precession motion of the ballooning mode structure induced by the flow-velocity shear. In Sec. III, the effect (i) is briefly explained by using equilibria with rigid toroidal rotations. As the Mach number of the flow is increased, the growth rate of the ballooning mode increases in the low-beta regime, whereas it decreases in the high-beta regime. Here the beta is a ratio of the plasma pressure to the magnetic pressure, and the Mach number is a ratio of the toroidal flow velocity to the ion thermal velocity. In Sec. IV, the effect (ii) is explained by using equilibria with sheared toroidal rotations. A precession motion of a ballooning structure along a magnetic field line is shown numerically and the periodically modulated exponential growth of the solution is discussed. The flow-velocity shear reduces the growth rates of the ballooning modes in the corresponding static equilibria by the averaging of the local equilibrium magnetic configuration which has both good and bad curvature regions in the toroi-

<sup>a)</sup>Present address: Naka Fusion Research Establishment, Japan Atomic Energy Research Institute, Naka, Ibaraki 311-0193, Japan.

dal geometry. In Sec. V, high- $n$  ballooning stability of realistic tokamak equilibria with reversed magnetic shear is studied. It is found that the ballooning mode becomes unstable for the larger flow-velocity-shear case in a low-aspect-ratio tokamak. This is understood by the change of the local magnetic configuration, and by the changes of both the mode structure and the potential function in the ballooning space. Conclusions are given in Sec. VI.

## II. TOKAMAK EQUILIBRIA AND BALLOONING EQUATIONS INCLUDING TOROIDAL FLOWS

MHD equilibria for tokamaks including toroidal flows are described by a second-order elliptic partial differential equation shown as<sup>15</sup>

$$\left( \frac{\partial^2}{\partial R^2} - \frac{1}{R} \frac{\partial}{\partial R} + \frac{\partial^2}{\partial Z^2} \right) \chi = -\mu_0 R^2 \frac{\partial p}{\partial \chi} \Big|_R - f \frac{df}{d\chi}. \quad (1)$$

Here  $(R, \phi, Z)$  are the cylindrical coordinates,  $\chi$  is the poloidal-flux function,  $p$  is the pressure,  $\mu_0$  is the vacuum permeability, and  $f \equiv RB_T$ , where  $B_T$  is the toroidal field. When the temperature is assumed as  $T = T(\chi)$ , then the pressure  $p$  is expressed as

$$p = \bar{p} \exp \left[ \frac{m_i \Omega^2 (R^2 - R_{ax}^2)}{2T} \right] = \bar{p} \exp \left[ M^2 \left( \frac{R^2}{R_{ax}^2} - 1 \right) \right]. \quad (2)$$

Here  $m_i$  is the ion mass,  $R_{ax}$  is the position of the magnetic axis,  $\bar{p} = \bar{p}(\chi)$  is the pressure at  $R = R_{ax}$  on each magnetic surface,  $\Omega = \Omega(\chi)$  is the angular rotation frequency of the toroidal flow, and  $M = M(\chi) \equiv v_T/v_{th}$  is the Mach number, where  $v_T \equiv R_{ax}\Omega$  and  $v_{th} \equiv \sqrt{2T/m_i}$ . It is noted that, if  $\Omega = 0$  is assumed, Eq. (1) becomes a Grad-Shafranov (G-S) equation. The effect of the toroidal flow is included only through the  $\partial p / \partial \chi|_R$  term in the generalized G-S equation (1). The MHD equilibria with toroidal flows studied in the present article are obtained by solving Eq. (1) numerically under the fixed boundary condition.<sup>14</sup> In this article, the ballooning stability is examined for these solutions.

The high- $n$  ballooning equations including toroidal flows can be derived from the linearized MHD equations.<sup>9,10</sup> A brief explanation of the derivation is given in the Appendix, and the final equations are written here:

$$\begin{aligned} & \rho B^2 \frac{\partial^2 \xi_{\parallel}}{\partial t^2} + 2\rho \Omega (\hat{\mathbf{k}} \cdot \hat{\mathbf{z}}) \frac{\partial \xi_{\perp}}{\partial t} + 2\rho \Omega (\nabla \Omega \cdot \hat{\mathbf{z}}) \xi_{\perp} \\ &= \mathbf{B} \cdot \nabla \left[ p C \left( \mathbf{B} \cdot \nabla \xi_{\parallel} + \frac{\mathbf{B} \cdot \nabla p}{p} \xi_{\parallel} - \frac{A}{p B^2} \xi_{\perp} \right) \right] \\ & \quad - C (\mathbf{B} \cdot \nabla p) \left( \mathbf{B} \cdot \nabla \xi_{\parallel} + \frac{\mathbf{B} \cdot \nabla p}{p} \xi_{\parallel} - \frac{A}{p B^2} \xi_{\perp} \right), \end{aligned} \quad (3)$$

$$\begin{aligned} & \rho |\hat{\mathbf{k}}|^2 \frac{\partial^2 \xi_{\perp}}{\partial t^2} + 2\rho (\hat{\mathbf{k}} \cdot \nabla \Omega) \frac{\partial \xi_{\perp}}{\partial t} - 2\rho \Omega B^2 (\hat{\mathbf{k}} \cdot \hat{\mathbf{z}}) \frac{\partial \xi_{\parallel}}{\partial t} \\ &= \frac{B^2}{\mu_0} \mathbf{B} \cdot \nabla \left( \frac{|\hat{\mathbf{k}}|^2}{B^2} \mathbf{B} \cdot \nabla \xi_{\perp} \right) \\ & \quad + C A \left( \mathbf{B} \cdot \nabla \xi_{\parallel} + \frac{\mathbf{B} \cdot \nabla p}{p} \xi_{\parallel} - \frac{A}{p B^2} \xi_{\perp} \right) + V \xi_{\perp}. \end{aligned} \quad (4)$$

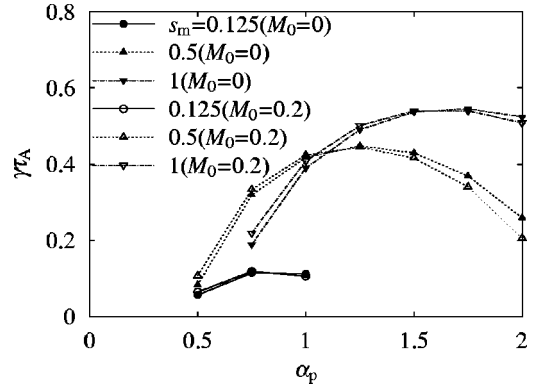


FIG. 1. Growth rates are plotted as a function of  $\alpha_p$  for  $s_m = 0.125, 0.5$  and  $1$ . The growth rate is larger for the equilibrium with the rigid rotation in the small- $\alpha_p$  regime, whereas it is larger for the static equilibrium in the large- $\alpha_p$  regime.

The notations in Eqs. (3) and (4) are referred to in the Appendix. The coefficients of Eqs. (3) and (4) are time-dependent through the scaled wave vector  $\hat{\mathbf{k}}$ . Thus  $\partial/\partial t$  cannot be replaced by  $i\omega$ . Therefore Eqs. (3) and (4) are solved as an initial-value problem.

## III. RIGID-ROTATION CASES

When a tokamak plasma is rotating toroidally, the plasma is pushed outward by the centrifugal force, which means that the toroidal flow effectively increases the driving force of the ballooning modes (pressure gradient) in the bad curvature region. In this section, the effective pressure gradient is seen by studying rigidly rotating tokamaks. It is noted that the coefficients of the ballooning equations become constant and the eigenmodes can be obtained.

The assumed Mach number and temperature profiles are  $M^2 = M_0^2 = \text{const}$  and  $T = T_0 = \text{const}$ . Then the rotation frequency  $\Omega$  is a constant, which corresponds to a rigid rotation. Here we pick up circular cross-section equilibria with the aspect ratio  $A = 10$ ,  $p(\hat{\chi}) = p_0(1 - \hat{\chi})$ , and  $q(\hat{\chi}) = 1 + q_1 \hat{\chi}^2$ . The parameters  $p_0$  and  $q_1$  are adjusted to give  $s_m = 0.125, 0.5$  and  $1$ , and  $\alpha_p = 1$  at the  $\hat{\chi} = 0.5$  surface, where  $s_m$  is the magnetic-shear parameter, and  $\alpha_p$  is the pressure-gradient parameter, which are defined as

$$s_m \equiv \frac{2\psi}{q} \frac{q'}{\psi'}, \quad (5)$$

$$\alpha_p \equiv -\sqrt{\frac{2\psi}{B_{T0}}} \frac{2\mu_0 q^2 p' R_{maj}}{B_{T0} \psi'}. \quad (6)$$

These expressions are consistent with the usual definitions of  $s \equiv r(dq/dr)/q$  and  $\alpha \equiv -2\mu_0 r^2(dp/dr)/R_{maj} B_P^2$  for large-aspect-ratio tokamaks<sup>16</sup> by assuming  $2\pi\psi \approx B_{T0}\pi r^2$  and  $q \approx r B_{T0}/R_{maj} B_P$ . Here  $B_{T0}$  is the vacuum toroidal field at the geometrical center of the plasma  $R = R_{maj}$ , and  $B_P$  is the poloidal magnetic field. In Eqs. (5) and (6), the prime denotes the derivative with respect to  $\hat{\chi}$ .

In Fig. 1, growth rates  $\gamma \tau_A$  at the  $\hat{\chi} = 0.5$  surface are plotted as a function of  $\alpha_p$  for various  $s_m$ . Here  $\tau_A \equiv R_{maj}/(B_{T0}/\sqrt{\mu_0 \rho_0})$  is the Alfvén time and  $\rho_0$  is the mass

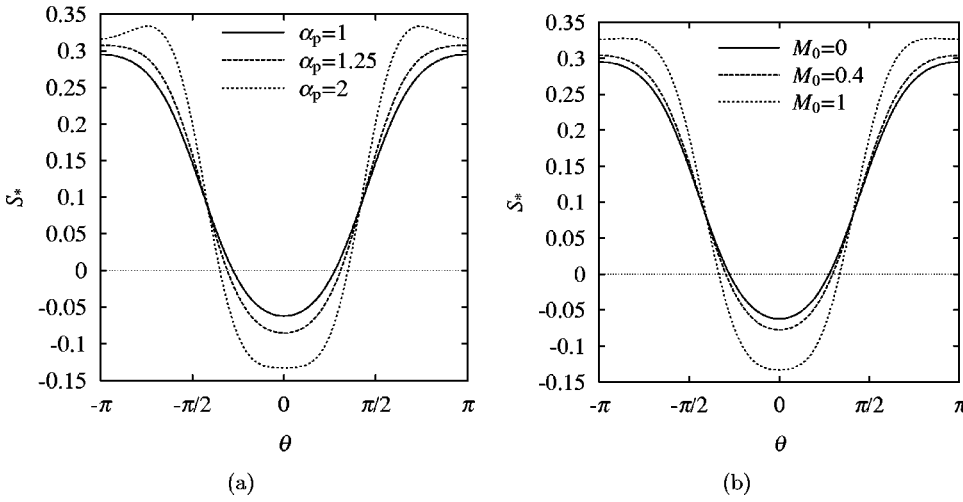


FIG. 2. Local magnetic shear  $S_*$  for equilibria with  $s_m = 0.5$ . The change of the local magnetic shear by varying  $M_0$  is similar to that by varying  $\alpha_p$  in static equilibria. (a) Pressure-gradient dependence (no flow). (b) Mach-number dependence.

density at the magnetic axis. It is noted that  $\theta_k = 0$  is assumed for simplicity. The growth rates are plotted for the static equilibria by filled symbols, and for the equilibria with rigid rotations of  $M_0 = 0.2$  by open symbols. It is seen that, for  $\alpha_p \approx 0.5$ , the growth rates are larger for the rigid-rotation case than those for the static case with the same  $s_m$ . For  $\alpha_p \approx 2$ , the situation is the opposite. It is considered that the equilibria with  $\alpha_p \approx 0.5$  are located near the first-stability boundary, and the growth rates are increased owing to the increase of the effective pressure gradient. The equilibria with  $\alpha_p \approx 2$  are located near the second-stability boundary, and the growth rates may be reduced by the change of the local magnetic shear which is related to the Shafranov shift enhanced by the centrifugal force of the toroidal flow.

For understanding the role of rigid rotation on the magnetic configuration, the local magnetic shear defined by<sup>17</sup>  $S_* \equiv -(\mathbf{B} \times \nabla \chi / |\nabla \chi|^2) \cdot \nabla \times (\mathbf{B} \times \nabla \chi / |\nabla \chi|^2)$  is shown in Fig. 2. Figure 2(a) shows  $S_*$  in the static equilibria with  $s_m = 0.5$  for  $\alpha_p = 1, 1.25$ , and  $2$ . Also Fig. 2(b) shows  $S_*$  in the equilibria with rigid rotations for  $M_0 = 0, 0.4$ , and  $1$ , where the magnetic-shear and pressure-gradient parameters are fixed at  $s_m = 0.5$  and  $\alpha_p = 1$ , respectively. The change of  $S_*$  by varying  $M_0$  is similar to that by varying  $\alpha_p$  in the static equilibria. Therefore, the behavior of the growth rates may be explained by the similar mechanism for realizing the second stability of ballooning modes.

The slight difference of the local magnetic shear between Figs. 2(a) and 2(b) is understandable. The effective pressure gradient is expressed as

$$\rho \mathbf{v} \cdot \nabla \mathbf{v} + \nabla p = \left[ \frac{d\bar{p}}{d\hat{\chi}} + \bar{p} \frac{dM^2}{d\hat{\chi}} \left( \frac{R^2}{R_{ax}^2} - 1 \right) \right] \times \exp \left[ M^2 \left( \frac{R^2}{R_{ax}^2} - 1 \right) \right] \nabla \hat{\chi}. \quad (7)$$

For equilibria with rigid rotations,  $\rho \mathbf{v} \cdot \nabla \mathbf{v} + \nabla p = (d\bar{p}/d\hat{\chi}) \exp[M^2(R^2/R_{ax}^2 - 1)] \nabla \hat{\chi}$ . Thus, the pressure gradient is effectively increased by the flow in the outer region of the torus. The change of pressure gradient is not constant on the entire magnetic surface.

#### IV. SHEARED-ROTATION CASES

In this section, effects of flow-velocity shear on growth rates of ballooning modes are discussed. In the high- $n$  ballooning equations (3) and (4), the coefficients are time dependent through the scaled wave vector  $\hat{\mathbf{k}}$ . It is noted that  $\hat{\mathbf{k}}$  becomes the same for the following two cases: (i)  $t = T$  and  $\vartheta = \Theta$  and (ii)  $t = T + \tau_d$  and  $\vartheta = \Theta + 2\pi$ , where  $T$  and  $\Theta$  are constants, and  $\tau_d \equiv 2\pi/\Omega$ . Therefore, solutions of Eqs. (3) and (4) seem to show periodic behavior.

Furthermore, the ballooning structure shows a precession motion along the magnetic field line.<sup>7-9,11</sup> Figure 3 shows a schematic explanation for the precession motion along the magnetic field line. The magnetic field lines labeled by ① and ② are located on neighboring magnetic surfaces. The magnetic-field structure has a shear. Toroidal flows on two magnetic surfaces also have different velocities as shown by the arrows. In deriving the high- $n$  ballooning equations,  $\mathbf{B} \cdot \nabla S = 0$  and  $dS/dt = 0$  have been assumed.

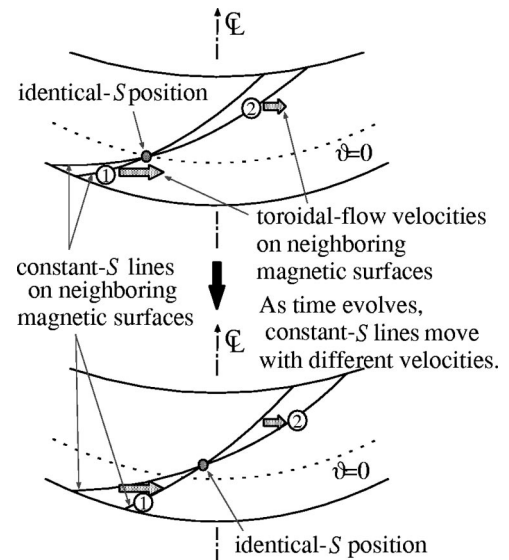


FIG. 3. A schematic explanation for the precession motion of the ballooning structure on the magnetic surface.



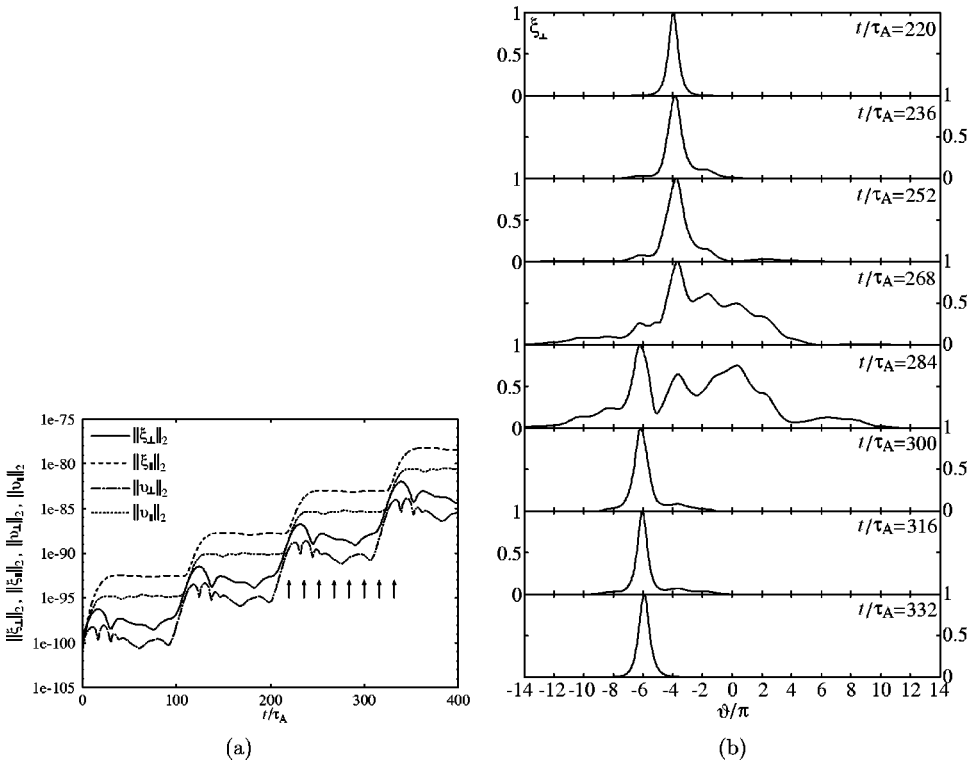


FIG. 4. Time evolution of perturbations is shown for  $s_m=1$ ,  $\alpha_p=1$ , and  $\Omega'\tau_A=0.0779$ . Periodically modulated exponential growth of the perturbed energy is seen in (a). The time evolution of mode structure is shown in (b), where the mode amplitude is normalized. (a) Time evolution of perturbed energy. (b) Mode structure at the times shown by the arrows in (a).

Therefore, the magnetic field line is identical to the constant- $S$  line. It is assumed that initially  $S$  on the line ① is equal to that on the line ② at  $\vartheta=0$ . As time evolves, the constant- $S$  lines move in the toroidal direction with different velocities, and the identical- $S$  position moves in the  $\vartheta$ -direction. Therefore, the precession motion of the ballooning structure occurs.

As the identical- $S$  position moves in the  $\vartheta$ -space, the ballooning mode feels the good and bad curvature alternatively. Since the mode grows in the bad curvature region, the destabilizing effect decreases when it moves to the good curvature region. Thus, the time evolution of the mode amplitude shows periodic behavior and the resultant growth rate may be reduced by the flow-velocity shear, which will be shown later in this work.

Since solutions of Eqs. (3) and (4) may not show a simple exponential growth for  $\Omega \neq 0$ , an appropriate definition of a growth rate is required. Here the energy of the perturbation is introduced as  $\tilde{E} \equiv \int d\vartheta (v_{\parallel}^2 + v_{\perp}^2 + \xi_{\parallel}^2 + \xi_{\perp}^2)$  and an instantaneous growth rate  $\Lambda(t)$  is given as

$$\Lambda(t) \equiv \frac{1}{2\tau_d} \frac{d}{dt} \ln \tilde{E}(t). \quad (8)$$

Then, the growth rate  $\gamma$  is defined as the time average of  $\Lambda(t)$  as

$$\gamma \equiv \frac{1}{t_1 - t_0} \int_{t_0}^{t_1} dt \Lambda(t), \quad (9)$$

where  $v_{\parallel} \equiv \partial \xi_{\parallel} / \partial t$ ,  $v_{\perp} \equiv \partial \xi_{\perp} / \partial t$ ,  $t_0$  is taken as the time when the time evolution of the perturbation enters the growth phase with periodic modulation, and  $t_1 = N\tau_d$ . Here  $N$  is an integer which is taken as large as possible.

For the equilibria studied in this section, the growth rates may be affected by both the flow-velocity shear and the change of the equilibrium magnetic configuration due to the toroidal flow.

First, circular cross-section equilibria with  $A=10$ ,  $\bar{p}(\hat{\chi}) = p_0(1 - \hat{\chi})$ , and  $q(\hat{\chi}) = q_0 + q_1\hat{\chi}^2$  are studied. The magnetic-shear parameter  $s_m$  and the pressure-gradient parameter  $\alpha_p$  are assumed as follows: (i)  $s_m=0.125$ ,  $\alpha_p=1$ , (ii)  $s_m=0.5$ ,  $\alpha_p=1$ , and (iii)  $s_m=1$ ,  $\alpha_p=1$ . In order to study the effect of flow-velocity shear, a particular flow profile is assumed. The Mach number and temperature profiles are assumed as  $M(\hat{\chi}) = M_0(1 - 2\hat{\chi})$  and  $T = \text{const}$ , respectively. Then the rotation frequency is  $\Omega = \Omega_0(1 - 2\hat{\chi})$ , and  $\Omega=0$  at the  $\hat{\chi}=0.5$  surface whereas  $\Omega' \neq 0$ . It is noted that the effective pressure gradient on the  $\hat{\chi}=0.5$  surface does not change by varying  $M_0$  from Eq. (7), although the local magnetic configuration at the  $\hat{\chi}=0.5$  surface is related to the other magnetic surfaces to maintain the global equilibrium.

As an example, time evolution of perturbations are shown in Fig. 4(a) for  $s_m=1$ ,  $\alpha_p=1$ , and  $\Omega'\tau_A=0.0779$ . The perturbed energy is given as  $\|X\|_2^2 \equiv \int d\vartheta X^2$ , where  $X$  represents  $\xi_{\perp}$ ,  $\xi_{\parallel}$ ,  $v_{\perp}$ , or  $v_{\parallel}$ . It is clearly seen that the perturbed quantities show a periodically modulated exponential growth. The period of the modulation is  $\tau_d/\tau_A \approx 107$  in this case. In Fig. 4(b), the associated time-dependent mode structure of  $\xi_{\perp}$  at the times shown by the arrows in Fig. 4(a) is plotted as a function of  $\vartheta$  during approximately one time period  $\tau_d$ . It is noted that  $\xi_{\perp}$  is normalized so that the maximum value of  $\xi_{\perp}$  is unity. At  $t/\tau_A \approx 220$ , the peak of  $\xi_{\perp}$  is located at a bad curvature region, whereas it moves  $-2\pi$  in the  $\vartheta$ -space at  $t/\tau_A \approx 332$ .

In Fig. 5, the growth rates  $\gamma\tau_A$  are plotted as a function

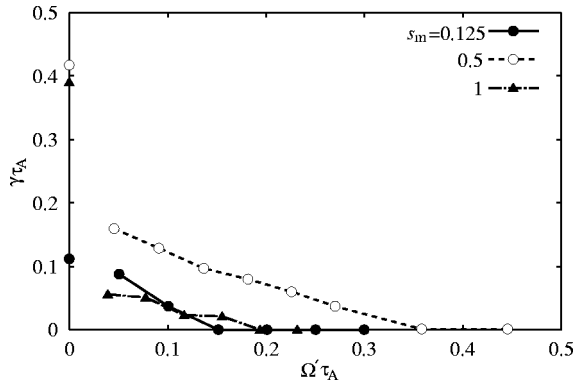


FIG. 5. Growth rates  $\gamma\tau_A$  are plotted as a function of  $\Omega'\tau_A$  for equilibria with sheared toroidal rotations. Magnetic-shear parameters are changed as  $s_m=0.125$ ,  $0.5$  and  $1$ , and the pressure-gradient parameter is fixed at  $\alpha_p=1$ . The ballooning modes are stabilized by the flow-velocity shear approximately greater than the growth rate in the static equilibria.

of  $\Omega'\tau_A$ , where  $\Omega'=d\Omega/d\hat{\chi}$ . It is noted that the definition of  $\gamma\tau_A$  is different between  $\Omega'\tau_A=0$  and  $\Omega'\tau_A\neq 0$ , and therefore  $\gamma\tau_A$  at  $\Omega'\tau_A=0$  is not connected with that for  $\Omega'\tau_A\neq 0$ . It is also noted that the calculation of  $\gamma\tau_A$  for smaller  $\Omega'\tau_A$  is time consuming in the initial value approach for the ballooning stability. It is seen that the ballooning modes are completely stabilized by the flow-velocity shear for  $\Omega'\tau_A$  larger than the growth rate for  $\Omega'\tau_A=0$  for  $s_m=0.125$ ,  $0.5$ , and  $1$ .

The reduction rate of  $\gamma\tau_A$  from that in the static equilibrium to that in the equilibria with small  $\Omega'\tau_A$  is the largest for  $s_m=1$ . The different behavior of the reduction rate of  $\gamma\tau_A$  may be understood from the localization of the mode structure. In the high-magnetic-shear case such as  $s_m=1$ , the mode structure is sufficiently localized in the  $\vartheta$ -space. Thus, the unstable mode feels only the bad curvature in the absence of the toroidal flow. When the precession motion occurs for  $\Omega'\tau_A\neq 0$ , the ballooning mode feels the good and bad curvature of the magnetic field line alternatively during the time evolution. Therefore the significant reduction of the growth rate is realizable even for relatively slow rotation. The mode

structure of  $\xi_\perp$  and the potential function given by  $-(V - CA^2/pB^2)\tau_A^2/\rho|\mathbf{k}|^2$  are shown in Fig. 6. Although the ballooning equations are a fourth-order system, the potential function is defined by viewing only the equation for  $\xi_\perp$ , Eq. (4), in a form  $\partial^2 \xi_\perp / \partial t^2 = (\text{second-order spacial derivative of } \xi_\perp) - (\text{potential function}) \times \xi_\perp + (\text{remaining terms})$  for simplicity. It is seen that the mode structure is localized in the region with negative potential function. The mode structure and the potential function are taken at  $t=3\tau_d$ , and are plotted with translation of  $3 \times 2\pi$  in the  $\vartheta$ -space for  $\Omega'\tau_A \neq 0$ . It is noted that the ballooning mode is moving in the  $-\vartheta$ -direction. For  $\Omega'\tau_A=0$ ,  $\xi_\perp$  is the eigenfunction. In this case, the mode structure and the potential both change slightly as  $\Omega'\tau_A$  is varied. The depth of the potential function becomes deeper and the width of the mode becomes narrower as  $\Omega'\tau_A$  is increased. It is considered that the ballooning stability is determined by the balance between the changes of the mode structure and the potential function.

On the other hand, in the low-magnetic-shear case,  $s_m=0.125$ , there is no significant reduction of  $\gamma\tau_A$ . It is noted that the mode structure is extended in the  $\vartheta$ -space for  $s_m=0.125$ . Thus the unstable mode already feels both good and bad curvature in the absence of the precession motion. Therefore, even if the precession motion occurs for  $\Omega'\tau_A \neq 0$ , the averaging effect due to the precession motion may be small. Therefore, it is considered that the stabilization mainly results from the change of the equilibrium magnetic field. In Fig. 7, the mode structure and the potential function are plotted as a function of  $\vartheta$  for  $s_m=0.125$  and  $\alpha_p=1$ . The mode structure and the potential function are taken at  $t=10\tau_d$  for  $\Omega'\tau_A \neq 0$ . Here the ballooning mode is moving in the  $-\vartheta$ -direction. It is noted that the mode structure and the potential function are plotted with translation of  $10 \times 2\pi$  in the  $\vartheta$ -space for  $\Omega'\tau_A \neq 0$ . As  $\Omega'\tau_A$  is varied, the potential function does not change substantially, whereas the mode structure changes significantly. The peak of the mode located at the minimum position of the potential function decreases as  $\Omega'\tau_A$  is increased. Therefore, stabilization is related to the change of the mode structure.

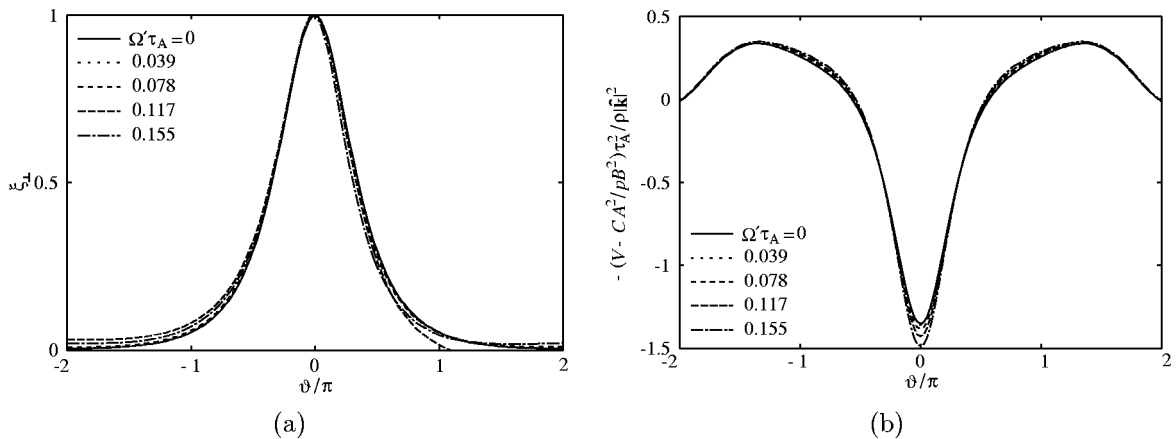


FIG. 6. Mode structure and potential function at  $t=3\tau_d$  are plotted as a function of  $\vartheta$  for  $s_m=1$  and  $\alpha_p=1$ . For  $\Omega'\tau_A=0$ ,  $\xi_\perp$  is the eigenfunction. Here the mode structure and the potential function are plotted with translation of  $3 \times 2\pi$  in the  $\vartheta$ -space for  $\Omega'\tau_A \neq 0$ . (a) Mode structure. (b) Potential function.

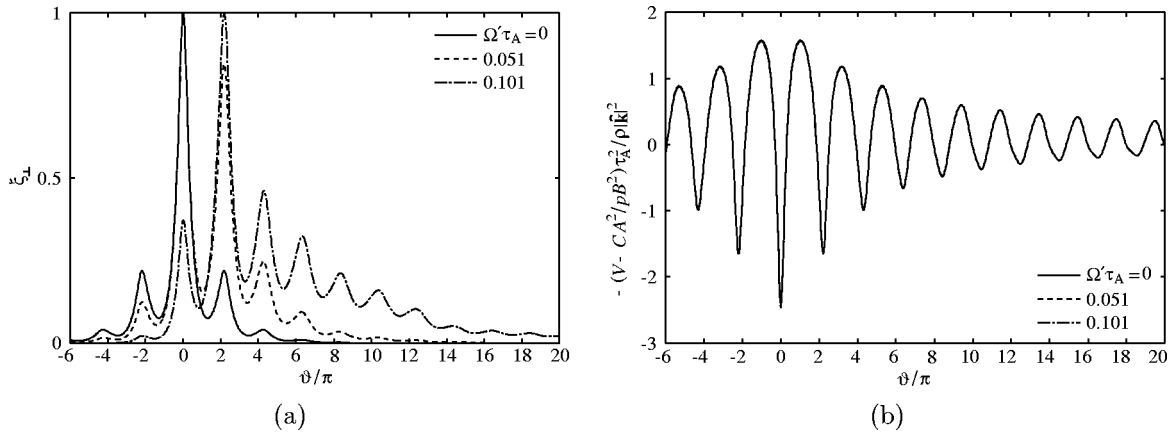


FIG. 7. Mode structure and potential function at  $t=10\tau_d$  are plotted as a function of  $\vartheta$  for  $s_m=0.125$  and  $\alpha_p=1$ . For  $\Omega'\tau_A=0$ ,  $\xi_\perp$  is the eigenfunction. Here the mode structure and the potential function are plotted with translation of  $10 \times 2\pi$  in the  $\vartheta$ -space for  $\Omega'\tau_A \neq 0$ . (a) Mode structure. (b) Potential function.

## V. REALISTIC-ASPECT-RATIO EQUILIBRIA WITH REVERSED MAGNETIC SHEAR

In a reversed-magnetic-shear equilibrium with an internal transport barrier (ITB), the steep pressure gradient is usually located in the small positive or negative-magnetic-shear region. Therefore, it is expected that high- $n$  ballooning modes are stable in this region. However, in the outer region with positive magnetic shear, they may become unstable. Also for H-mode plasmas, stability analysis of ballooning modes becomes important in the edge region. Here we consider the former case and discuss the stability of ballooning modes in the region with positive magnetic shear.

The aspect ratios of the equilibria studied here are  $A=1.5$  and  $3$ . The ellipticity is  $\kappa=1.54$ , and the triangularity is  $\delta=0.2$ . The central toroidal beta is assumed to be  $\beta_{T0} \equiv 2\mu_0 p_0/B_{T0}^2 = 20.7\%$  for  $A=1.5$ , and  $\beta_{T0}=5\%$  for  $A=3$ .

The profiles of pressure  $\bar{p}$ , square of Mach number  $M^2$ , and temperature  $T$  are given as follows:  $\bar{p} \propto \tanh[5(\hat{\chi}-0.25)]$ ,  $M^2 \propto \tanh[12(\hat{\chi}-0.25)]$ , and  $T \propto \tanh[2(\hat{\chi}-0.25)]$ . When the Mach number is varied, the  $M^2$  profile is fixed and the value at the magnetic axis is changed. The safety factor  $q$  at the magnetic axis is  $q_0=10$ , the minimum value is  $q_{\min}=2.1$  at  $\hat{\chi}=0.35$ , and the edge value of safety factor is  $q_a=5$ . In the following, the results of the stability calculations are shown, which are carried out at the  $\hat{\chi}=0.45$  surface.

In Fig. 8, the growth rates are plotted as a function of  $\Omega'\tau_A$ . For  $A=3$ , it is seen that the unstable ballooning mode is stabilized for  $\Omega'\tau_A \geq 0.03$ . It is noted that  $\gamma\tau_A=0.059$  for the static equilibrium. The result is similar to the high-magnetic-shear case in Sec. IV. The flow-velocity shear of  $\Omega'\tau_A=0.03$  corresponds to  $M_0=0.2$  for the assumed flow profile, which has been obtained in experiments. It is noted that the magnetic-shear parameter is about 0.88, and the mode structure is well localized around the bad curvature region.

For  $A=1.5$ , the ballooning mode becomes unstable by increasing  $\Omega'\tau_A$ . It is noted that the ballooning mode is stable for the static equilibrium. To understand the reason for the behavior of the growth rate, the high- $n$  ballooning equation without a flow

$$\mathbf{B} \cdot \nabla \left( \frac{|\hat{\mathbf{k}}|^2}{B^2} \mathbf{B} \cdot \nabla \xi_\perp \right) + \left[ \frac{2\mu_0}{B^4} (\mathbf{B} \times \hat{\mathbf{k}} \cdot \nabla p) (\mathbf{B} \times \hat{\mathbf{k}} \cdot \boldsymbol{\kappa}) + \frac{\mu_0 \rho |\hat{\mathbf{k}}|^2}{B^2} \omega^2 \right] \xi_\perp = 0 \quad (10)$$

is solved with magnetic configurations of the equilibria including toroidal flows. Here  $\omega$  is a frequency. For small  $\Omega'\tau_A$ , the precession motion of a ballooning mode is slow, thus the behavior of the mode is considered to be approximately the same as in the static case with  $\theta_k = \Omega t$  for each instance. It is noted that the pressure gradient is fixed at the value of the static equilibrium. In the equilibria with flows, the pressure gradient is effectively increased. Thus the driving force may be estimated smaller in the calculations for the rotating equilibria. In Fig. 9, the growth rate is plotted as a function of  $\theta_k$  for various  $\Omega'\tau_A$ . It is noted that the ballooning mode is stable for  $\Omega'\tau_A \leq 0.056$ . As  $\Omega'\tau_A$  is increased, the unstable region in  $\theta_k$  increases, and also the growth rate increases. Therefore, this may be related to the appearance of the instability around  $0.07 \leq \Omega'\tau_A \leq 0.111$ .

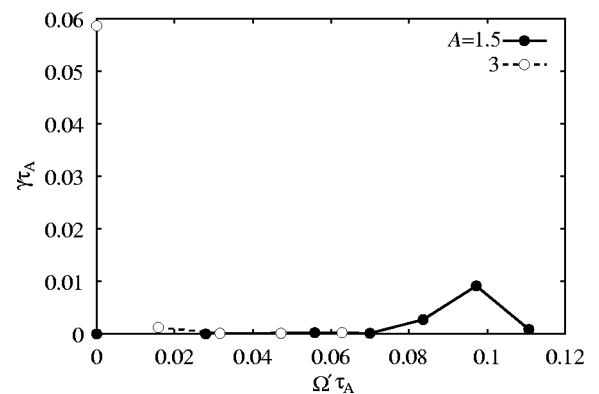


FIG. 8. Growth rates are plotted as a function of  $\Omega'\tau_A$  at the  $\hat{\chi}=0.45$  surface for the  $A=1.5$  and  $3$  equilibria with reversed magnetic shear. For  $A=3$ , the high- $n$  ballooning mode unstable for  $\Omega'\tau_A=0$  is stabilized by a shear flow with relatively small  $\Omega'\tau_A$ . However, for  $A=1.5$ , the ballooning mode becomes unstable for large  $\Omega'\tau_A$ .



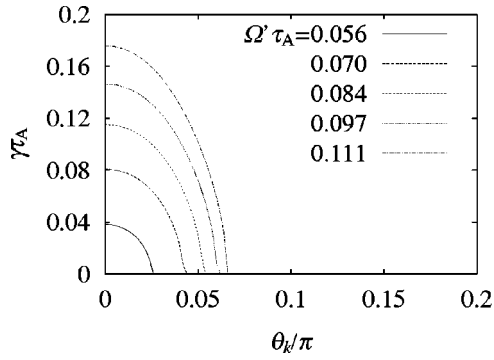


FIG. 9. Incompressible high- $n$  ballooning equation for static equilibria is solved by using magnetic configurations of rotating equilibria, and the growth rate is obtained as a function of  $\theta_k$ . The pressure gradient is fixed at the value of the static equilibrium.

If the growth rate  $\gamma\tau_A$  in Fig. 8 is approximated by the  $\theta_k$ -average of  $\gamma\tau_A$  in Fig. 9, i.e.,  $\gamma\tau_A$  (in Fig. 8)  $\approx (1/2\pi) \oint d\theta_k \gamma\tau_A$  (in Fig. 9), then  $\gamma\tau_A$  in Fig. 8 is expected to become large as  $\Omega'\tau_A$  is increased. However,  $\gamma\tau_A$  in Fig. 8 is decreased for  $\Omega'\tau_A \gtrsim 0.1$ . Thus the flow shear must have any stabilizing effect other than the averaging effect of the magnetic configuration.

In Fig. 10, the mode structure and the potential function at  $t = 5\tau_d$  are plotted as a function of  $\vartheta$ . The ballooning mode structure for  $\Omega'\tau_A \neq 0$  is moving in the  $-\vartheta$ -direction, and it is plotted with translation of  $5 \times 2\pi$  in the  $\vartheta$ -space. The mode structure is sufficiently localized in the bad curvature region. Therefore, the behavior of the mode structure and the potential function is similar to the high-magnetic-shear case in Sec. IV. The width of the mode becomes narrower and the depth of the potential becomes deeper as  $\Omega'\tau_A$  is increased. The ballooning stability is determined by these changes. Furthermore, the space-averaged potential function weighted by  $\xi_\perp$ , given by  $\|\xi_\perp (V - CA^2/\rho B^2)\tau_A^2/\rho|\hat{\mathbf{k}}|^2\|_1 / \|\xi_\perp\|_1$ , is shown in Fig. 11. Here  $\|X\|_1 \equiv \int d\vartheta X$ . This quantity may be related to the growth rate of the perturbed energy, since the perturbed energy is a space-integrated quantity. In fact, the role of the space-averaged potential function is decreasing as  $\Omega'\tau_A$  is increased. Therefore, the stabilization around

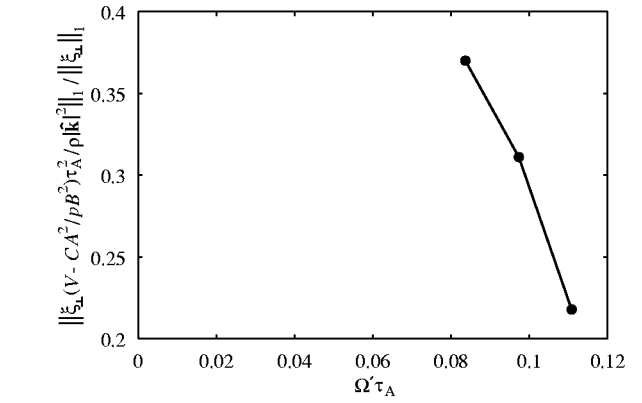
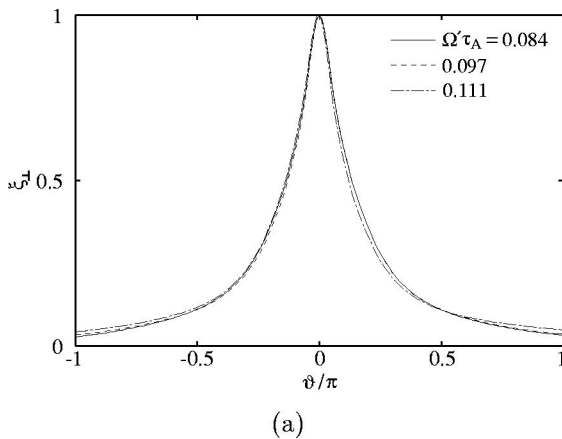


FIG. 11. Space-averaged potential function for high- $n$  ballooning modes is plotted as a function of  $\Omega'\tau_A$  for  $A=1.5$ . The space-averaged potential function decreases as  $\Omega'\tau_A$  is increased, which may be related to the stabilization at  $\Omega'\tau_A \approx 0.111$ .

$\Omega'\tau_A \approx 0.111$  is understandable by the changes of the mode structure and the potential function due to the shear flow.

## VI. CONCLUSIONS

The effects of toroidal flows on high- $n$  ballooning modes have been studied. When the time-dependent eikonal representation is used for the perturbations, the ballooning mode exhibits a precession motion along the magnetic field line and the perturbed energy shows a periodically modulated exponential growth.

The effects of toroidal flow come from two parts: (i) the effective pressure gradient due to the centrifugal force of the toroidal flow and the corresponding change of the equilibrium magnetic configuration, and (ii) the averaging effect of the local magnetic configuration due to the flow-velocity shear.

In order to examine these effects separately, the equilibria with rigid rotations have been studied first. In this case, the effect of the flow-velocity shear is absent. As the Mach number is increased, the effective pressure gradient increases, and the growth rate increases in the low-beta regime whereas it decreases in the high-beta regime. This behavior

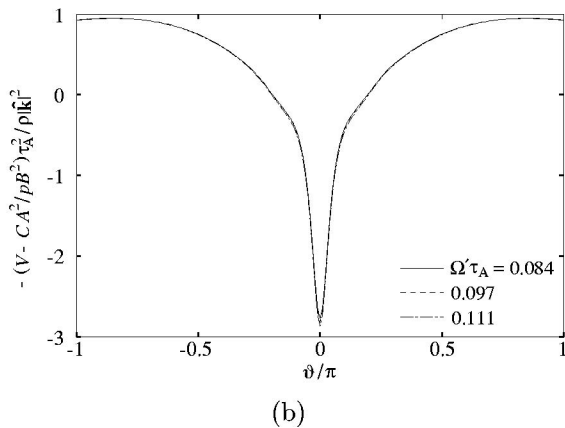


FIG. 10. Mode structure and potential function at  $t = 5\tau_d$  are plotted as a function of  $\vartheta$  for  $A = 1.5$ . It is noted that the mode structure and the potential function are plotted with translation of  $5 \times 2\pi$  in the  $\vartheta$ -space. (a) Mode structure. (b) Potential function.

of the growth rate can be explained by the similar mechanism for realizing the second stability of ballooning modes.

In the presence of flow-velocity shear, the growth rate is defined by the time average of the temporal evolution of the perturbed energy for the period of the precession motion over  $2\pi$  in the  $\vartheta$ -space. The mode feels not only bad curvature but also good curvature as a result of the precession motion. Therefore, the growth rate becomes smaller than that for the static equilibrium. The reduction of the growth rate due to the averaging effect of the precession motion becomes larger for equilibria with higher magnetic shear, since the mode structure is localized in the bad curvature region. In the low-magnetic-shear case, however, the mode structure is already extended in a wide region in the  $\vartheta$ -space even for the static case. Therefore, even if the precession motion is induced, the growth rate may not be reduced significantly.

In addition to the averaging effect by the flow-velocity shear, the growth rate of the ballooning mode is affected by the changes of the mode structure and the potential function as shown in Fig. 6 for the high-magnetic-shear case. In the low-magnetic-shear case, the change of the potential function by varying the flow-velocity shear is not significant, and the stabilization is caused by the change of the mode structure as shown in Fig. 7.

As a realistic example, the ballooning stability of D-shaped equilibria with reversed magnetic shear has been studied. Here the pressure and the Mach number have strong gradient in the core region. In the region where the magnetic shear is negative, the ballooning modes are stable. However, at the region slightly farther out than the  $q_{\min}$  surface, the ballooning modes become unstable. For a conventional tokamak with  $A=3$ , it has been shown that the ballooning mode which is unstable in the static equilibrium can be stabilized by the flow-velocity shear. Here the mode structure is sufficiently localized, and the situation is similar to the high-magnetic-shear case explained in Sec. IV.

For a low-aspect-ratio tokamak with  $A=1.5$ , it has been found that the ballooning instabilities appear for larger  $\Omega'\tau_A$ . It is considered that the behavior of the growth rate is explained by the change of the local magnetic configuration, and by the changes of the mode structure and the potential function. When the static ballooning equation is solved, the unstable- $\theta_k$  region increases as  $\Omega'\tau_A$  is increased as shown in Fig. 9. On the other hand, it is also found that the space-averaged potential function for the ballooning mode is decreasing as  $\Omega'\tau_A$  is increased for  $\Omega'\tau_A \geq 0.084-0.111$  as shown in Fig. 11.

It is noted that this instability is not induced by the Kelvin–Helmholtz drive, since the second-order derivative of flow velocity is not included in the present analysis. Tatsuno *et al.* have studied interchange instabilities in a slab plasma with a shear flow.<sup>18</sup> They have shown that the combined effect of shear flow mixing and Alfvén wave propagation overcomes the instability driving force asymptotically. It is considered that the stabilization of the ballooning modes for large  $\Omega'\tau_A$  is also related to this mechanism.

## ACKNOWLEDGMENTS

The authors thank Dr. T. Tatsuno, Dr. S. Tokuda, and Dr. H. Sugama for useful suggestions and discussions.

## APPENDIX: BALLOONING EQUATIONS INCLUDING TOROIDAL FLOWS

It is known that linearized MHD equations including equilibrium plasma flows can be reduced to the Frieman–Rotenberg (F–R) equation<sup>19</sup>

$$\rho \frac{\partial^2 \xi}{\partial t^2} + 2\rho \mathbf{v} \cdot \nabla \frac{\partial \xi}{\partial t} = \mathcal{F}(\xi), \quad (\text{A1})$$

where

$$\begin{aligned} \mathcal{F}(\xi) = & \frac{1}{\mu_0} (\nabla \times \mathbf{Q}) \times \mathbf{B} + \frac{1}{\mu_0} (\nabla \times \mathbf{B}) \times \mathbf{Q} + \nabla \cdot (\gamma p \nabla \cdot \xi \\ & + \xi \cdot \nabla p) + \nabla \cdot (\rho \xi \mathbf{v} \cdot \nabla \mathbf{v} - \rho \mathbf{v} \mathbf{v} \cdot \nabla \xi), \end{aligned} \quad (\text{A2})$$

$$\mathbf{Q} = \nabla \times (\xi \times \mathbf{B}). \quad (\text{A3})$$

Here  $\mathbf{B}$  and  $\mathbf{v}$  are the equilibrium magnetic field and flow velocity, respectively,  $\rho$  and  $p$  are the mass density and pressure, respectively,  $\gamma$  is the specific heat ratio, and  $\xi$  is the Lagrangian displacement vector.

High- $n$  ballooning equations for MHD equilibria including purely toroidal flows are derived from the F–R equation<sup>9</sup> by using an eikonal representation for  $\xi$  shown as

$$\xi(\hat{\chi}, \vartheta, \alpha, t) = \hat{\xi}(\hat{\chi}, \vartheta, t) e^{inS(\hat{\chi}, \alpha, t)}, \quad (\text{A4})$$

where  $n$  is the toroidal mode number,  $S$  is the eikonal, and the wave vector is defined as  $\mathbf{k} = \nabla S$ . The coordinates  $(\hat{\chi}, \vartheta, \alpha)$  are introduced for the covering space. By using these coordinates, the magnetic field is expressed as  $\mathbf{B} = -\chi' \nabla \hat{\chi} \times \nabla \alpha$ . Here the prime denotes the derivative with respect to  $\hat{\chi}$ . The radial coordinate  $\hat{\chi}$  is defined as the normalized poloidal flux ( $\hat{\chi}=0$  at the magnetic axis and  $\hat{\chi}=1$  at the plasma edge),  $\vartheta$  is the extended poloidal angle, and  $\alpha$  is the coordinate labeling magnetic field lines. It is noted that the domain of  $\vartheta$  is  $-\infty < \vartheta < \infty$ , which is called a covering space. By using the usual magnetic coordinates, the magnetic field is expressed as  $\mathbf{B} = \psi' \nabla \hat{\chi} \times \nabla \theta + \chi' \nabla \zeta \times \nabla \hat{\chi}$ , where  $\psi$  is the toroidal-flux function and  $\theta$  ( $\zeta$ ) is the poloidal (toroidal) angle, which increases  $2\pi$  along the short (long) way around the torus. The toroidal angle  $\zeta$  is related to  $\phi$  by  $\zeta = -\phi$  for giving a positive-definite Jacobian. The relations between  $(\theta, \zeta)$  and  $(\vartheta, \alpha)$  are given by  $\vartheta = \theta$  and  $\alpha = \zeta - q\theta$ , where  $q \equiv d\psi/d\chi$  is a safety factor.

The eikonal  $S$  is assumed to satisfy<sup>7</sup>

$$\mathbf{B} \cdot \nabla S = 0, \quad (\text{A5})$$

$$\frac{dS}{dt} = 0, \quad (\text{A6})$$

since the perturbation satisfying Eqs. (A5) and (A6) may be most dangerous. The toroidal flow velocity is given by  $\mathbf{v} = -R^2 \Omega \nabla \zeta$ . According to Ref. 7,  $S = k_a(\alpha + \Omega t) + k_q q$  and

$\mathbf{k} = \nabla S = k_\alpha \nabla \alpha + (k_q + k_\alpha \dot{\Omega} t) \nabla q$  are chosen, where  $\dot{\Omega} \equiv d\Omega/dq$ . With the scaled wave vector  $\hat{\mathbf{k}} \equiv \mathbf{k}/k_\alpha$  and the ballooning angle  $\theta_k \equiv k_q/k_\alpha$ ,  $\hat{\mathbf{k}}$  is given by

$$\hat{\mathbf{k}} = \nabla \zeta - q \nabla \theta - (\theta - \theta_k - \dot{\Omega} t) \nabla q. \quad (\text{A7})$$

Substituting Eq. (A4) into Eq. (A1) and collecting  $\mathcal{O}(n^2)$  terms yield  $\hat{\xi} \cdot \nabla S = 0$  for  $n \gg 1$ . Thus  $\hat{\xi}$  is shown as

$$\hat{\xi} = \hat{\xi}^{(0)} + \frac{i}{n} \hat{\xi}^{(1)}, \quad (\text{A8})$$

where

$$\hat{\xi}^{(0)} \equiv \xi_\perp \frac{\mathbf{B} \times \nabla S}{B^2 k_\alpha} + \xi_\parallel \mathbf{B}, \quad (\text{A9})$$

$$\hat{\xi}^{(1)} \equiv \xi_k \frac{\nabla S}{|\nabla S|^2}. \quad (\text{A10})$$

Using Eqs. (A8)–(A10) and collecting  $\mathcal{O}(n)$  terms yield

$$\begin{aligned} \xi_k = \frac{1}{B^2/\mu_0 + \gamma p} \left\{ -\frac{1}{\mu_0} \mathbf{B} \cdot [\nabla \times (\hat{\xi}^{(0)} \times \mathbf{B})] \right. \\ \left. + \gamma p \nabla \cdot \hat{\xi}^{(0)} + \hat{\xi}^{(0)} \cdot \nabla p \right\}. \end{aligned} \quad (\text{A11})$$

By collecting  $\mathcal{O}(1)$  terms,

$$\begin{aligned} \rho \frac{\partial^2 \hat{\xi}^{(0)}}{\partial t^2} + 2\rho \mathbf{v} \cdot \nabla \frac{\partial \hat{\xi}^{(0)}}{\partial t} + \rho \mathbf{v} \cdot \nabla (\mathbf{v} \cdot \nabla \hat{\xi}^{(0)}) \\ = \frac{1}{\mu_0} (\nabla \times \hat{\mathbf{Q}}) \times \mathbf{B} + \frac{1}{\mu_0} (\nabla \times \mathbf{B}) \times \hat{\mathbf{Q}} \\ + \nabla (\gamma p \nabla \cdot \hat{\xi}^{(0)} + \hat{\xi}^{(0)} \cdot \nabla p) + \hat{\xi}^{(0)} \cdot \nabla (\rho \mathbf{v} \cdot \nabla \mathbf{v}) \\ + (\nabla \cdot \hat{\xi}^{(0)}) \rho \mathbf{v} \cdot \nabla \mathbf{v} + \frac{1}{\mu_0} \{ \mathbf{B} \cdot [\nabla \times (\hat{\xi}^{(1)} \times \mathbf{B})] \nabla S \\ - \mathbf{B} \times [\nabla \times (\xi_k \mathbf{B})] - \xi_k \mathbf{B} \times (\nabla \times \mathbf{B}) \} - \nabla (\gamma p \xi_k) \\ - \gamma p (\nabla \cdot \hat{\xi}^{(1)}) \nabla S - (\hat{\xi}^{(1)} \cdot \nabla p) \nabla S - \rho \xi_k \mathbf{v} \cdot \nabla \mathbf{v} \end{aligned} \quad (\text{A12})$$

and

$$\hat{\mathbf{Q}} \equiv \nabla \times (\hat{\xi}^{(0)} \times \mathbf{B}) = \nabla \xi_\perp \times \hat{\mathbf{k}} \quad (\text{A13})$$

are obtained.

Here closed high- $n$  ballooning equations are obtained for the variables  $\xi_\parallel$  and  $\xi_\perp$  by calculating the  $\mathbf{B}$  and  $\mathbf{B} \times \hat{\mathbf{k}}$  components of Eq. (A12) as

$$\begin{aligned} \rho B^2 \frac{\partial^2 \xi_\parallel}{\partial t^2} + 2\rho \Omega (\hat{\mathbf{k}} \cdot \hat{\mathbf{Z}}) \frac{\partial \xi_\perp}{\partial t} + 2\rho \Omega (\nabla \Omega \cdot \hat{\mathbf{Z}}) \xi_\perp \\ = \mathbf{B} \cdot \nabla \left[ p C \left( \mathbf{B} \cdot \nabla \xi_\parallel + \frac{\mathbf{B} \cdot \nabla p}{p} \xi_\parallel - \frac{A}{p B^2} \xi_\perp \right) \right] \\ - C (\mathbf{B} \cdot \nabla p) \left( \mathbf{B} \cdot \nabla \xi_\parallel + \frac{\mathbf{B} \cdot \nabla p}{p} \xi_\parallel - \frac{A}{p B^2} \xi_\perp \right), \end{aligned} \quad (\text{A14})$$

$$\begin{aligned} \rho |\hat{\mathbf{k}}|^2 \frac{\partial^2 \xi_\perp}{\partial t^2} + 2\rho (\hat{\mathbf{k}} \cdot \nabla \Omega) \frac{\partial \xi_\perp}{\partial t} - 2\rho \Omega B^2 (\hat{\mathbf{k}} \cdot \hat{\mathbf{Z}}) \frac{\partial \xi_\parallel}{\partial t} \\ = \frac{B^2}{\mu_0} \mathbf{B} \cdot \nabla \left( \frac{|\hat{\mathbf{k}}|^2}{B^2} \mathbf{B} \cdot \nabla \xi_\perp \right) \\ + C A \left( \mathbf{B} \cdot \nabla \xi_\parallel + \frac{\mathbf{B} \cdot \nabla p}{p} \xi_\parallel - \frac{A}{p B^2} \xi_\perp \right) + V \xi_\perp, \end{aligned} \quad (\text{A15})$$

where

$$A(\chi, \vartheta, t) \equiv (\mathbf{B} \times \hat{\mathbf{k}}) \cdot (2p\kappa - \rho R \Omega^2 \hat{\mathbf{R}}), \quad (\text{A16})$$

$$\begin{aligned} V(\chi, \vartheta, t) \equiv (\mathbf{B} \times \hat{\mathbf{k}}) \cdot \left[ 2 \frac{\partial p}{\partial \chi} \Big|_R \kappa - \frac{\partial (\rho R^2 \Omega^2)}{\partial \chi} \Big|_R \frac{\hat{\mathbf{R}}}{R} \right. \\ \left. + \frac{2\rho \Omega}{B^2} \frac{d\Omega}{d\chi} (\mathbf{B} \cdot \hat{\mathbf{Z}}) \nabla \chi \right], \end{aligned} \quad (\text{A17})$$

$$C(\chi, \vartheta) \equiv \frac{B^2/\mu_0}{B^2/\mu_0 + p}. \quad (\text{A18})$$

Here  $\hat{\mathbf{R}}$  and  $\hat{\mathbf{Z}}$  are the unit vectors in the directions of  $R$  and  $Z$ , respectively, and  $\kappa \equiv (\mathbf{B}/B) \cdot \nabla (\mathbf{B}/B)$  is the curvature of the magnetic field. It is noted that  $\gamma = 1$  is assumed for simplicity. Equations (A14) and (A15) are the same as Eqs. (3) and (4).

<sup>1</sup>S. D. Scott, P. H. Diamond, R. J. Fonck *et al.*, Phys. Rev. Lett. **64**, 531 (1990).

<sup>2</sup>L. L. Lao, K. H. Burrell, T. S. Casper *et al.*, Phys. Plasmas **3**, 1951 (1996).

<sup>3</sup>T. Fujita, Y. Kamada, S. Ishida *et al.*, Nucl. Fusion **39**, 1627 (1999).

<sup>4</sup>J. W. Connor, R. J. Hastie, and J. B. Taylor, Phys. Rev. Lett. **40**, 396 (1978).

<sup>5</sup>R. L. Dewar and A. H. Glasser, Phys. Fluids **26**, 3038 (1983).

<sup>6</sup>J. M. Greene and M. S. Chance, Nucl. Fusion **21**, 453 (1981).

<sup>7</sup>W. A. Cooper, Plasma Phys. Controlled Fusion **30**, 1805 (1988).

<sup>8</sup>E. Hameiri and S. T. Chun, Phys. Rev. A **41**, 1186 (1990).

<sup>9</sup>F. L. Waelbroeck and L. Chen, Phys. Fluids B **3**, 601 (1991).

<sup>10</sup>K. Grassie and M. Krech, Phys. Fluids B **2**, 536 (1990).

<sup>11</sup>R. L. Miller, F. L. Waelbroeck, A. B. Hassam, and R. E. Waltz, Phys. Plasmas **2**, 3676 (1995).

<sup>12</sup>K. Grassie and M. Krech, Phys. Fluids B **2**, 1864 (1990).

<sup>13</sup>V. D. Shafranov, *Reviews of Plasma Physics* (Consultants Bureau, New York, 1966), Vol. 2.

<sup>14</sup>M. Furukawa, Y. Nakamura, S. Hamaguchi, and M. Wakatani, J. Plasma Fusion Res. **76**, 937 (2000).

<sup>15</sup>E. Hameiri, Phys. Fluids **26**, 230 (1983).

<sup>16</sup>J. P. Freidberg, *Ideal Magnetohydrodynamics* (Plenum, New York, 1987).

<sup>17</sup>R. D. Hazeltine and J. D. Meiss, Phys. Rep. **121**, 1 (1985).

<sup>18</sup>T. Tatsuno, F. Volponi, and Z. Yoshida, Phys. Plasmas **8**, 399 (2001).

<sup>19</sup>E. Frieman and M. Rotenberg, Rev. Mod. Phys. **32**, 898 (1960).